Dalton Transactions

ROYAL SOCIETY OF CHEMISTRY

PAPER

View Article Online
View Journal | View Issue

Cite this: *Dalton Trans.*, 2022, **51**, 10601

Design of a D_{3h}-symmetry prismatic tris-(ferrocene-1,1′-diyl) molecular cage bearing boronate ester linkages†

Maurycy Krzyżanowski, [a] Anna M. Nowicka, [b] Krzysztof Kazimierczuk, [c] Krzysztof Durka, [a] Sergiusz Luliński [a] and Artur Kasprzak *[a]

Received 26th April 2022,
Accepted 19th June 2022

DOI: 10.1039/d2dt01306a

rsc.li/dalton

This paper presents a simple, highly selective, and efficient (isolated yield of 68%) synthesis of a novel D_{3h}-symmetry prismatic tris-(ferrocene-1,1′-diyl) organic cage (**FcB-cage**) by incorporating a boronate ester as a linkage motif. 1,1′-Diboronated derivatives of ferrocene and 2,3,6,7,10,11-hexahydroxytriphenylene (**HHTP**) were used as the starting materials. The synthesized cage was comprehensively characterized by spectroscopic and microscopic methods, powder X-ray diffraction, thermogravimetry and voltammetry. Cyclic voltammetry analysis revealed the electronic communication between the ferrocene units of the **FcB-cage**. In addition, to better understand the mechanism behind the synthesis of such a cage, as well as its geometric properties, we performed DFT calculations.

Introduction

Boronic esters are among the most widely used linkage motifs in the synthesis of highly organized structures, *e.g.*, covalent organic frameworks (COFs).[1–5] In fact, some of the first COFs were synthesized by polycondensation of diboronic acids and 2,3,6,7,10,11-hexahydroxytriphenylene (**HHTP**).[6] The usefulness of boronic ester linkages stems from their D_{2h} symmetry and the thermodynamically favoured esterification reaction.[7] In the synthesis of COFs, one starting material is a knot component, whilst the other is the linker. The starting materials are often rigid, planar, and aromatic organic building blocks commonly featuring the D_{2h}, D_{3d}, D_{4h}, or D_{6h} symmetry.[8] In recent years, COFs have gathered much attention because of their interesting features, such as designable crystalline structure.[9–11] For example, a hexagonal, honey-comb-like 2D COF can be constructed *via* the condensation reaction of two molecules, one having the D_{3d} symmetry and the other having the D_{2h} symmetry.[12] COFs are not, however, limited to only 2D sheets. For example, when one of the building blocks has a T_d symmetry, 3D COFs can be obtained.[13]

Alternatively, it was demonstrated that discrete organic cages could be synthesized instead of COFs using different starting materials that induce the 3D geometry.[14–17] Such cages are commonly porous organic materials. Their synthesis usually employs imine bond formations, based on the reaction between amine and aldehyde components. In fact, imine motifs are also frequently used in COF synthesis. Interestingly, it was demonstrated that the COF material could be obtained instead of a respective organic cage molecule upon changing the aldehyde component, *e.g.*, the planar and aromatic dialdehyde featuring the D_{2h} symmetry.[18] This is just another example of the close relationship between COFs and organic cages, as simply changing the symmetry of building blocks can lead to a COF or a cage. The utility of boronate esters in such chemistry has been demonstrated and toughly reviewed in recent years.[19,20] For example, the [2 + 2] type condensation of 1,1′-ferrocenediboronic acid (**1**) with pentaerythritol was used by Aldridge to generate a dimeric macrocycle,[21] whilst Kobayashi and co-workers reported the usage of bis(catechol) linkages toward the synthesis of boronate containing capsules[22] (see Fig. 1). In addition, regarding the different types of organic cages, it is important to differentiate between organic and metal–organic cages. The latter ones utilize the metal-ligand coordination bonds, which induces the desired geometry.[23] There are various examples of utilizing boronate ester groups for the construction of organic[24–26] and metal–organic boronate ester cages.[27]

Ferrocene is one of the more interesting building blocks of organic cages. Recently, it has been demonstrated that organic cages derived from 1,1′-diformylferrocene can be easily and

[a]*Faculty of Chemistry, Warsaw University of Technology, Noakowskiego Str. 3, 00-664 Warsaw, Poland. E-mail: artur.kasprzak@pw.edu.pl, akasprzak@ch.pw.edu.pl*
[b]*Faculty of Chemistry, University of Warsaw, Pasteura Str. 1, 02-093 Warsaw, Poland*
[c]*Centre of New Technologies, University of Warsaw, Banacha 2C, 02-097 Warsaw, Poland*

†Electronic supplementary information (ESI) available: Optimalization experiments, spectral characterization, additional discussion on machine learning, thermal properties, SEM data, and theoretical calculations. See DOI: https://doi.org/10.1039/d2dt01306a

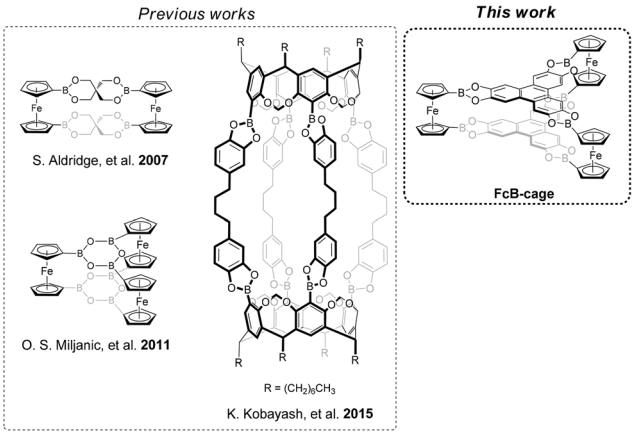

Fig. 1 Examples of previous organized molecules bearing a boronated ester linkage[21,22,33] and the aim of this work.

effectively synthesized by means of the imine bond formation reaction with C_3-symmetric aromatic amines.[28,29] Such an organic cage can be viewed as two parallel 2D sheets connected *via* a linkage that is perpendicular to those sheets. More specifically, the two parallel 2D sheets are rigid aromatic frameworks, while the three linkages are the ferrocene units. Taking into account that ferrocene itself is composed of two planar cyclopentadienyl (Cp) units linked together *via* an iron cation perpendicular to them, it is a highly geometry-inducing starting material that enables the synthesis of organic cages. Such ferrocene-containing organic cages are of interest not only because they are redox-active[30,31] but also because they may share some properties with their COF counterparts such as sensing ability[32] or gas storage.[17]

Planar and highly symmetrical organic cages comprising boronate ester linkages have not been reported yet, with the boroxine-containing organic cage (see Fig. 1)[33] being the most similar reported molecule of that type. Taking into account the recently reported usefulness of 1,1′-disubstituted ferrocene derivatives, which strongly induce the formation of organic cages, this work aimed at selective synthesizing an organic cage (**FcB-cage**; Scheme 1) derived from **HHTP** and **1** by means of a boronate ester formation. Density functional theory (DFT) calculations were performed to better understand the structure of a cage and rationalize the thermodynamic advantages of its formation over the oligomeric structures.

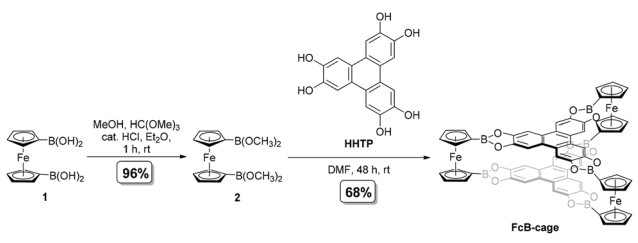

Scheme 1 Synthesis of the **FcB-cage** under optimized conditions.

Results and discussion

Synthesis of FcB-cage

The synthesis of **FcB-cage** under optimized conditions is presented in Scheme 1. At first, the trials were performed with **1** (3 equivalents) and **HHTP** (2 equivalents). Inspired by the reports of the synthesis of **HHTP** derived COFs,[3,5,34] 1,4-dioxane/mesitylene (1/1 v/v) was used as a solvent system (for the optimization experiments, see section 1, ESI†). We expected that the product shall precipitate from the reaction mixture. No formation of the product was, however, observed after stirring the reagents at room temperature for several days. Changing the temperature to 85 °C also did not result in the formation of the **FcB-cage** and once again only starting materials were recovered. Attempts to synthesize the **FcB-cage** by applying the reported procedures for the synthesis of other ferrocene containing organic cages, which employed methanol or ethanol as the solvent,[28,29] were also unsuccessful (in the recovery of starting materials). We suspected that the difficulties in dissolving **1** or **HHTP** could be the culprit behind those above-discussed unsatisfactory results. Therefore, the subsequent trials were performed in the solvent that had been earlier proved to dissolve both the starting materials, namely *N*,*N*-dimethylformamide (DMF). To our delight, in this case, a precipitate was formed. However, there appeared to be a significant concentration threshold equal to 10 mM (with the respect to compound **1**). In other words, when the concentration of compound **1** was 1, 2, 4, or 8 mM, the formation of a precipitate was not observed. While DMF enabled the partial formation of the cage, the reaction yield was relatively low (*ca.* 40%), and the presence of oligomers in the sample was observed (see section 1, ESI†). We suspected that it resulted from the poor solubility of the intermediate products in DMF. In fact, the formation of organized organic cages requires the good solubility of the starting materials and the intermediate products in the reaction solvent. In order to omit those limitations, 1,1′-bis(dimethoxyboryl)ferrocene (**2**), a methanol ester derivative of **1**, was used in the next trials, which is far more soluble than **1**.

The reported synthesis of **2** involved the metathesis of 1,1′-bis(dibromoboryl)ferrocene with methoxytrimethylsilane.[35] To avoid the use of hazardous boron tribromide we developed a more convenient route which uses the easily accessible and air-stable **1**[33] as the starting material (Scheme 1). We were pleased to find that the esterification of $B(OH)_2$ groups with methanol proceeded readily in Et_2O at room temperature upon the addition of trimethyl orthoformate and a catalytic amount of HCl (a few drops of a 2 M ethereal solution). The addition of $HC(OMe)_3$ was essential for shifting the equilibrium towards the product as it reacts with water formed during esterification. Overall, the process resembles the formation of dimethyl acetals or ketals from respective carbonyl derivatives. It could also be potentially valuable for the synthesis of other boronic esters. It should be noted that product **2** was obtained as a viscous red oil which is prone to rapid hydrolysis in contact with water and moist air resulting in the recovery of **1**.

The solubility of **2** in common organic solvents was incredibly better than **1**. The synthesis of the target **FcB-cage** from **2** and **HHTP** was carried out in DMF at room temperature. The molar concentrations of the starting materials were 11.5 mM (3 equiv.) and 7.7 mM (2 equiv.) for **2** and **HHTP**, respectively. Under optimized conditions, we were able to obtain the **FcB-cage** in good yield (68%). It is worth noting that the protocol is easy-to-perform; the reaction set-up was simple, as the reactants were placed in a flask, and then the solvent was added. In addition, the target **FcB-cage** precipitated from the reaction mixture and was then washed with DMF and acetone to remove the unreacted starting materials and impurities. In addition, we tested a mechanochemical synthesis of the **FcB-cage** from **1** and **HHTP** in a ball mill using the liquid-assisted grinding technique (a drop of DMF was added). However, PXRD analysis revealed that **1** did not undergo reaction under such conditions.

Characterization of FcB-cage

The **FcB-cage** was found to be practically insoluble in any solvent. The ^{1}H NMR spectrum of the **FcB-cage** in DMSO-d_6 measured immediately after sample preparation comprised peaks coming from the building blocks of the **FcB-cage**, namely 1,1′-ferrocenediboronic acid (**1**) and **HHTP**. We suspected that it resulted from the boronate esters being sensitive to the presence of water, which causes their hydrolysis to the parent boronic acid and alcohol (diol). When the spectrum was measured after stirring the **FcB-cage** in DMSO-d_6 for 24 hours at room temperature in air (see the Experimental section), the intensity of those peaks increased (Fig. S1, ESI†), which supported our hypothesis of the hydrolysis of boronate ester linkages forming the **FcB-cage** (no products of partial hydrolysis of the cage were observed). Interestingly, the peak integrals suggested that the molar ratio of the building blocks is 3 : 2 (**1** : **HHTP**). This molar ratio is in good agreement with the proposed structure of the **FcB-cage**. High-resolution mass spectrometry (HRMS) further supported the successful synthesis of the **FcB-cage** (Fig. S3, ESI†). Importantly, HRMS analysis suggested that the sample did not contain any high- or low-mass oligomeric side-products.

We performed solid-state NMR experiments to gain deeper insights into the structural features of the **FcB-cage**. The ^{13}C MAS NMR spectrum of the **FcB-cage** generally agrees with the expectations (Fig. 2). Due to signal broadening and the relatively small difference in the chemical shifts of non-equivalent carbon of Cp rings, it is impossible to distinguish their separate resonances. Thus, the spectrum shows one intense resonance of ferrocenyl carbon atoms centred at 77.5 ppm. In contrast, one can easily assign the signal at 108.6 ppm to the carbon atoms of the **HHTP** linker located at the *ortho* positions with respect to the O-bound carbons.[36] In addition, the spectrum shows the resonances at 128.2 and 150.4 ppm, which can be unambiguously assigned to the quaternary carbon atoms of the central ring of **HHTP** and the peripheral O-bound carbon atoms of this linker, respectively. The ^{11}B MAS NMR spectrum of the **FcB-cage** shows a single symmetrical resonance centred

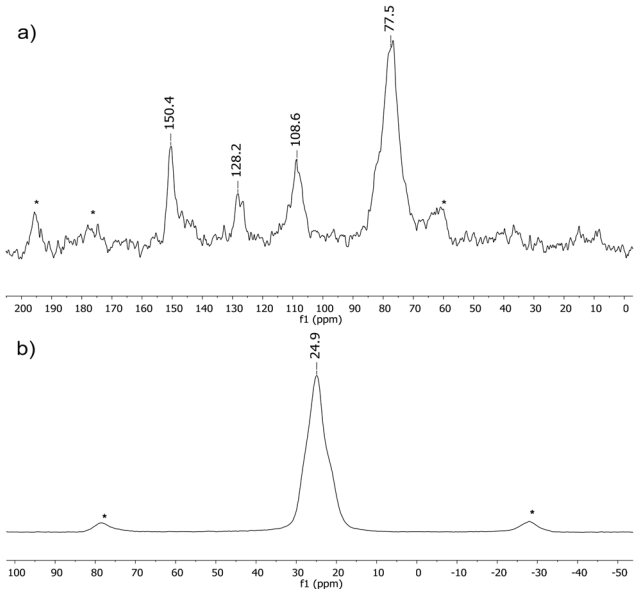

Fig. 2 ^{13}C (a) and ^{11}B MAS NMR (b) spectra of the **FcB-cage** (spinning frequency 12 kHz, spinning sidebands are marked with asterisks).

at 24.9 ppm (Fig. 2). It confirms the presence of boronate groups as it essentially resembles signals typically observed for arylboronic acids and esters under isotropic conditions (*ca.* 25–30 ppm).[37] A closer inspection reveals shoulders at both sides of the signal which may point to slight differences in boron shielding; this effect may be attributed to a different environment of the boron atoms at the periphery of the crystallites.

Attenuated total reflectance Fourier-transform infrared (ATR-FT-IR) spectroscopy provided further insights into the **FcB-cage** structure. The ATR-FT-IR spectrum of the **FcB-cage** (Fig. S4, ESI†) shows a strong broadband of B–O stretching vibrations at 1360 cm^{-1}. Although there are some literature examples in which the authors were able to define a particular shift in this region and distinguish between boronic esters, boronic acids or boroxines,[38] in the **FcB-cage** the interpretation is rather ambiguous. The band splits into several components, which may be attributed to the overlap with the B–C stretching vibrations or the results from the deviation of the **FcB-cage** from the D_{3h} symmetry. The latter hypothesis is also supported by the observation of the ATR-FT-IR pattern in the 1000–1070 cm^{-1} region. The appearance of moderately strong sharp bands is expected for boronic esters, whereas in the case of **FcB-cage** the bands are broad and split into several signals. The more diagnostic vibrational mode, that has been conserved in the 640–680 cm^{-1} range for most boronic esters, involves the out-of-plane movements of the boron and oxygen atoms. This characteristic band is indeed observed at 670 cm^{-1} and its assignment was unambiguously confirmed by DFT calculations. Nonetheless, this band typically splits into several sharp peaks for boronic esters, while in the case of the **FcB-cage** it is slightly broadened and jagged.

The above-discussed absorption bands in the ATR-FT-IR spectrum of the **FcB-cage** suggest that a boronate ester structure was indeed formed. However, because the direct interpretation is ambiguous at some points, a machine learning technique was applied.[39–41] For this purpose, the SVM (support vector machines) model with rbf (radial basis function) kernels was used (Fig. S5, ESI†).[42] The details of the machine learning technique and the crucial parameters dealing with this analysis are presented in section 3, ESI.† The dataset consisted of 28 different molecules, all of them being boronate ester or boroxine derivatives.[38] Hyperparameters present in the SVM model with rbf kernels are: regularization constant (C) and kernel hyperparameter (γ). In order to find the most optimal values of those hyperparameters, a grid search was performed. The best parameters were found to be 0.001 for the γ parameter and 1 for C. Even when disregarding the characteristic band in the range of 1015–1069 cm^{-1}, 100% accuracy was achieved. Despite the fact that the differences between the IR spectra of boroxines and boronic esters are quite subtle, the respective signals can be grouped into clusters, thus easily differentiating both types of compounds. After the classifying algorithm had been successfully established, we could move on to classify the IR signal of the product. Because exactly four values of frequencies need to be extracted from the spectrum, the values were determined by firstly extracting all values of the signal in the area of interest, and then averaging those values, which resulted in mean frequencies that have values of 1387, 1321, 1246 and 680 cm^{-1}. The applied classifying algorithm predicted that the product is an ester with a 67% probability. When incorporating the characteristic signal, the probability grew to 88%.

Powder X-ray diffraction (PXRD) pattern (Fig. 3) points to an ordered, micro- or nanocrystalline character of the **FcB-cage** due to the presence of several relatively sharp peaks in the 2θ range of 4–20°. Pawley refinement allowed to index all of the observed peaks (Fig. S18, ESI†), *i.e.*, there were no additional peaks left, indicating that the sample is homogeneous and is not contaminated by unreacted substrates. This is in accordance with the SEM analysis showing uniform nanocrystallites which strongly point to phase homogeneity. The volume of the proposed monoclinic cell is 3522 $Å^3$ which roughly corresponds to the volume of two molecules of the **FcB-cage** (V = 1715 $Å^3$). In addition, the size of those nanocrystallites estimated using the Scherrer equation is *ca.* 30–40 nm which is roughly in agreement with their width range measured based on the scanning electron microscopy (SEM) images (Fig. 3). Thus, it can be claimed that the outcomes of the PXRD and SEM analyses are highly consistent and thus the presence of oligomeric species in the **FcB-cage** sample is unlikely. Lastly, it is worth noting that the energy-dispersive X-ray spectroscopy analysis confirmed the presence of expected atoms in the molecular formula of the **FcB-cage** (for data see Table S2, ESI†).

The thermal stability of the **FcB-cage** was investigated under a N_2 atmosphere by thermogravimetric analysis (TGA) (Fig. S9, ESI†). A slow continuous mass loss (*ca.* 7%) is observed below 300 °C. It is presumably due to the removal of traces of moisture and solvents. Overall, the material exhibits a relatively high thermal resistance in agreement with its compact structure composed of aromatic building blocks. In addition, the material exhibits long-term stability under ambient conditions as the PXRD pattern of a sample remained essentially unchanged after several months. A more significant (*ca.* 20%) mass loss of the molecular structure occurs in the temperature range of 400–600 °C. It is accompanied by the exothermic peak of the DSC curve with the maximum at *ca.* 550 °C indicating that the degradation of the material presumably resulted from the thermolysis of B–C bonds.

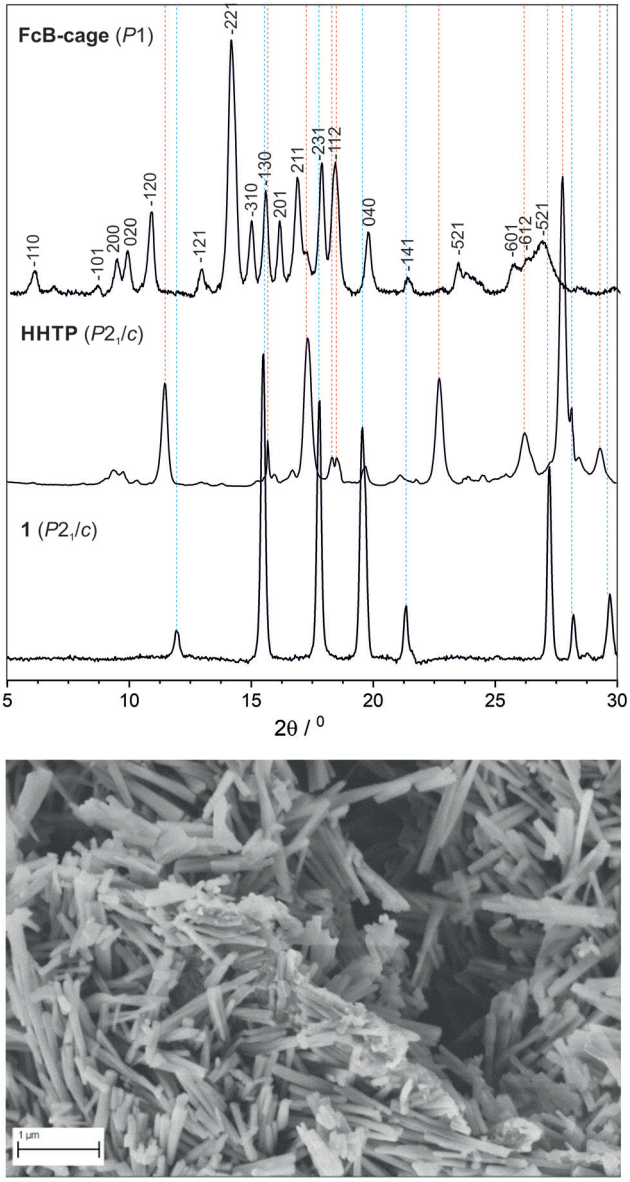

Fig. 3 (top) PXRD pattern of the **FcB-cage** with peaks indexed using the Pawley refinement method (crystal system: monoclinic, space group: $P2$, unit cell: a = 21.02 Å, b = 18.08 Å, c = 10.27 Å, β = 115.5°, V = 3522 $Å^3$, χ^2 = 2.6) together with the PXRD pattern for substrates (**HHTP** and **1**). (bottom) Representative SEM image of the **FcB-cage** nanocystalline material.

The results of the elemental analysis of the **FcB-cage** were consistent with the expected elemental composition of the sample. Small differences between the calculated and found values originate from the hygroscopic nature of the **FcB-cage** resulting in the presence of water in the sample. The presence of water in the **FcB-cage** sample can be clearly observed in the TGA thermogram (Fig. S9, ESI†). It is worth noting that commercially available **HHTP**, used as the reactant in the synthesis of **FcB-cage**, also contains some amount of water. The results of the elemental analysis suggested the presence of 5 molecules of water in the formula (for the **FcB-cage**: calcd for $C_{66}H_{36}B_6Fe_3O_{12}$: C, 63.25; H, 2.90; for **FcB-cage** + **5H$_2$O**: calcd for $C_{66}H_{46}B_6Fe_3O_{17}$: C, 59.00; H, 3.45, found: C, 58.86; H, 3.35). The estimated content of water from TGA is 6.97 wt%. The content of water in the sample calculated from the above-listed formula is *ca.* 7.18 wt%. Thus, the content of water estimated by elemental analysis and TGA are in good agreement. Slight differences result from the different methods of sample preparation for the analysis.

To study the electrochemical properties of the **FcB-cage**, electrochemical analyzes were performed in anhydrous dimethylsulfoxide (DMSO) with the addition of 0.10 M of tetrabutylammonium hexafluorophosphate ($TBAPF_6$) as a supporting electrolyte. Before the experiment, the electrode surface was modified with the **FcB-cage**. The electrochemical characteristics of the modified electrode (GC/**FcB-cage**-$TBABF_4$-Nafion®) were obtained using cyclic voltammetry at various electrode scan rates ranging from 0.002 to 0.4 V s^{-1}. The obtained voltammograms are presented in Fig. 4. The obtained voltammetric curves are characterized by the three pairs of current peaks (E_{Ox}/E_{Red}: 0.67 V/0.18 V; 0.96 V/0.53 V and 1.20 V/0.82 V) that correspond to the three ferrocene units present in the **FcB-cage** structure. It should be stressed that the poor current signal separation (especially in the anodic region, see inset in Fig. 4) is a consequence of the strong coordinating properties of PF_6^- anions,[43–45] and the separation of those peaks declined with increasing scan rate. The HOMO energy level calculated on the basis of the first oxidation potential is −5.71 eV, which is in agreement with the DFT-calculated value of −5.78 eV. For comparison, the anodic and cathodic peaks for the one electron redox process for native ferrocene are centred at 0.42 V (E_{Ox}) and 0.33 V (E_{Red}),[46] for 1,1′-ferrocenediboronic acid (**1**) at *ca.* 0.2 V (E_{Ox}) and *ca.* 0.17 V (E_{Red}),[47] whilst for 1,1′-ferrocenediboronic acid bis-pinacol ester at. 0.31 V (E_{Ox}) and *ca.* 0.28 V (E_{Red}).[48] In addition, the existence of several current peaks for 1,1′-ferrocenediboronic acid derived dimeric structures has been previously observed, such as in the case of dimers comprising indacene based tetrol units (E_{Ox}/E_{Red}: 0.23 V/*ca.*0.20 V and 0.39 V/*ca.*0.35 V).[48] For the **FcB-cage**, the cathodic signals are better defined than the anodic signals. Moreover, the presence of three pairs of current signals indicates the electronic communication between ferrocene units in the **FcB-cage**. We consider that electronic communication is transferred through bonding by triphenylene core as the electronic effect of redox processes for each boronated ferrocene unit. This is also reflected by the much higher first oxidative potential of the **FcB-cage** with respect to ferro-

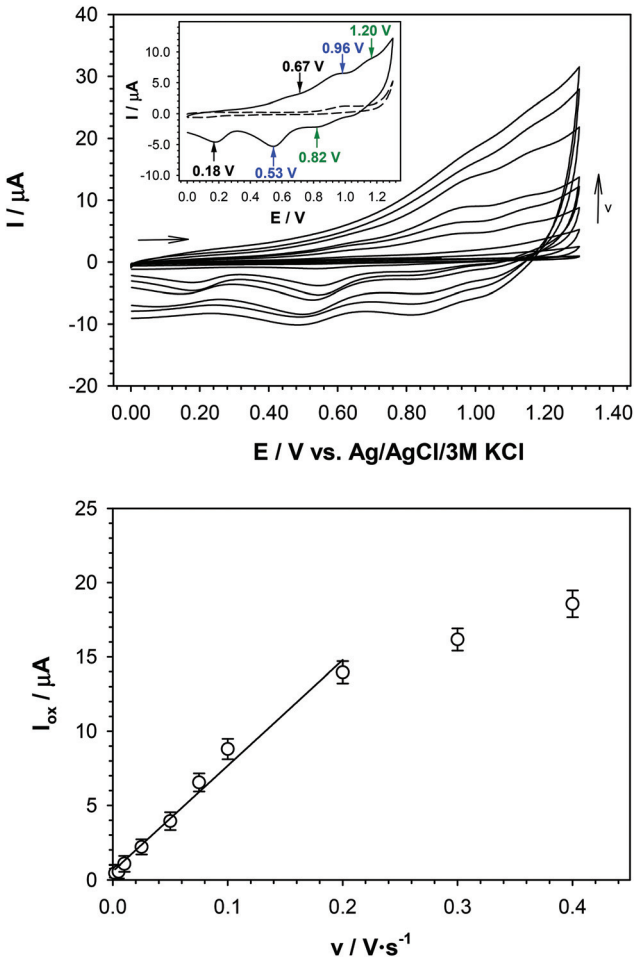

Fig. 4 (top) Cyclic voltammograms of the GC/**FcB-cage**-$TBABF_4$-Nafion® recorded in anhydrous DMSO at various scan rates. Top inset: CV voltammogram in the presence at v = 50 mV s^{-1}. Experimental conditions: $C_{FcB-cage}$ = 5 mM, C_{TBAPF6} = 0.10 M, T = 21 °C. (bottom) Plot of the **FcB-cage** oxidation currents at 1.0 V *versus* the scan rate.

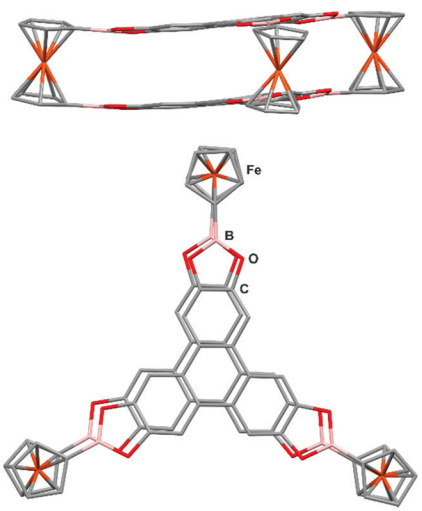

Fig. 5 DFT-optimized structure of the **FcB-cage** viewed from two different perspectives.

cene and its 1,1′-diboronic derivatives. In general, the introduction of the boron atom to the ferrocene unit decreases the E_{ox} value. In contrast the removal of one electron in the **FcB-cage** requires higher energy. At the same time the reverse electrochemical processes, *i.e.* reduction of respective cationic states, are kinetically hampered leading to the large hysteresis effect. These observations can be explained in terms of the resonance effect between the ferrocene units induced by their close distance, parallel orientation, flat geometry of the boron coordination sphere and the π-electron conducting properties of the **HHTP** linker. This effect was not observed for the dimeric structures comprising 1,1′-diboronated ferrocene and indacene-based tetraol units due to the aliphatic nature of the latter component.

Finally, due to the fact that the **FcB-cage** was immobilized on the electrode surface, its electrode process should be a surface process. In order to confirm this hypothesis, the dependence of the oxidation signal intensity as a function of the electrode scan rate was plotted and the obtained dependencies are presented in the inset graph of Fig. 4 (bottom). The linear dependence $I = f(v)$ indicates the surface electrode process.

Theoretical insights into the formation of the FcB-cage

The molecular structure of the **FcB-cage** was established on the basis of DFT calculations. The B97D functional with the 6-311++G(d,p) basis set was selected as it can accurately describe the π–π interactions between the **HHTP** aromatic units. Although the B3LYP functional is more frequently used than B97D, it falsely predicts the dispersion interactions between **HHTP** units. The single-molecule optimization of the **FcB-cage** shows that the molecule deviates from its initial D_{3h} symmetry (Fig. 5). This is manifested by the slight puckering of the

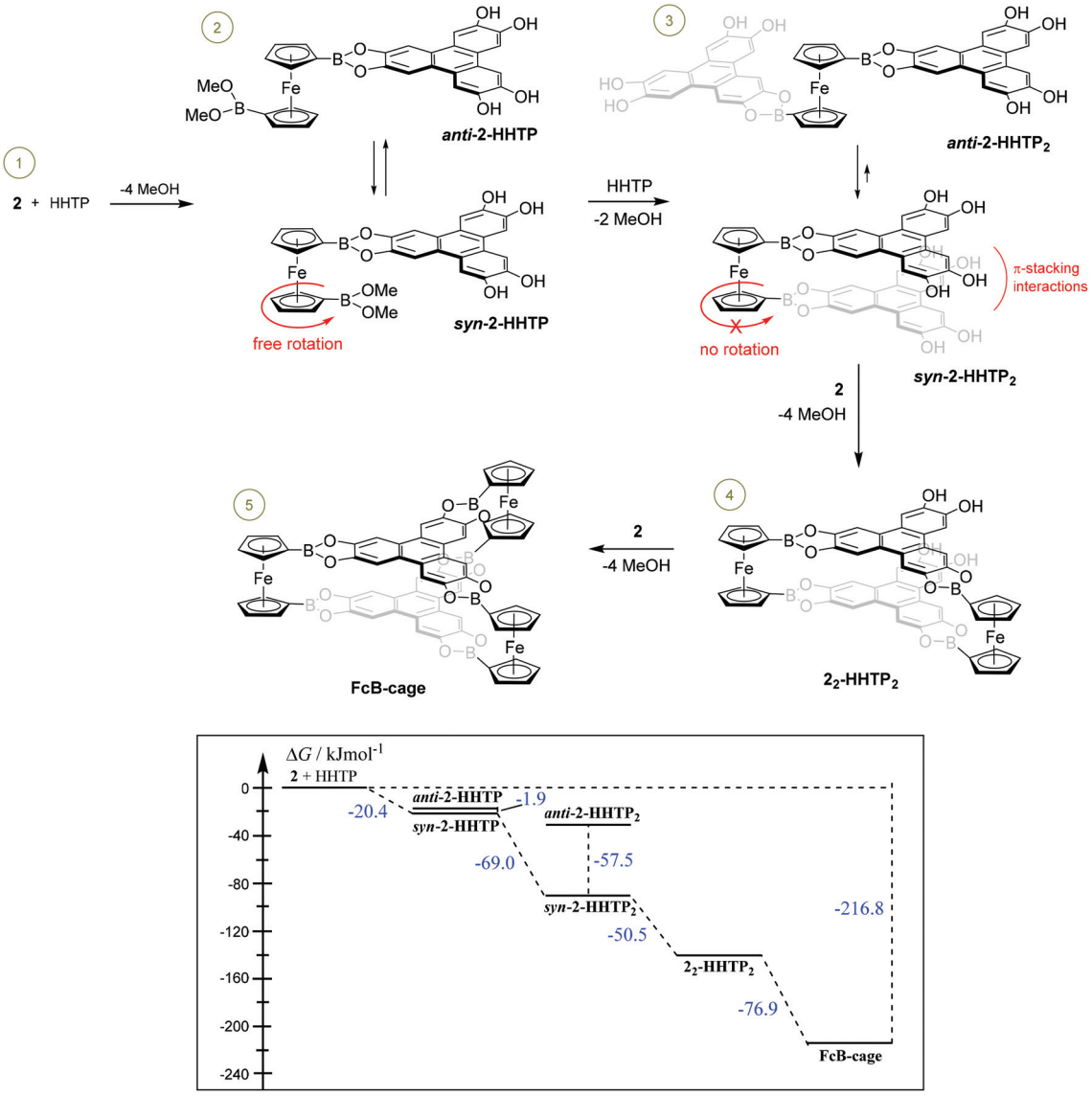

Scheme 2 Proposed mechanism for the formation of the **FcB-cage** together with the energy diagram (presented in the frame).

HHTP moieties, twisting of the ferrocene units with respect to the **HHTP** planes and the deflection of the C–B bonds from the Cp rings. Such molecular deformations enable the in-plane shifting of the **HHTP** units by 0.117 Å ensuring more advantageous π-stacking interactions. For comparison, the in-plane shifting of two independent π-stacking **HHTP** molecules optimized at the same level of theory is 0.387 Å. The intramolecular distance between the root-mean-square **HHTP** planes in the **FcB-cage** is 3.311 Å, which is close to the value obtained for the **HHTP** dimer (3.184 Å). The Cp rings in the ferrocene moieties adopt nearly eclipsed conformation. The slight twist of the Cp rings enhances the formation of the complementary pairs of B···O interactions between parallel boronic units, although further calculations indicate that they provide a marginal contribution to the total stabilization energy of the cage. In a subsequent step, the intramolecular interaction energy between **HHTP** units was calculated by extracting the ferrocene moieties from the structure. In such a discrete dimeric pair, the boron atoms were terminated with hydrogen atoms, while the positions of the remaining atoms were preserved from the optimized molecule **FcB-cage**. The BSSE-corrected interaction energy is 87.0 kJ mol^{-1}. Thus the π-stacking interactions provide a very important contribution to the total stabilization of the **FcB-cage** structure.

It can be expected that the formation of the **FcB-cage** proceeds in several successive steps (see Scheme 2). At first, the molecule of **HHTP** reacts with molecule **2** to produce the **2-HHTP** adduct with ΔG = −20.4 kJ mol^{-1}. The rotation of the Cp rings is not hampered as the energy difference between the two extreme conformers, namely *syn*-**2-HHTP** and *anti*-**2-HHTP**, is only 1.9 kJ mol^{-1}. The reaction of **2-HHTP** with another **HHTP** molecule to give **2-HHTP$_2$** is thermodynamically highly favoured due to the dispersive interactions between the **HHTP** moieties (ΔG = −69.0 kJ mol^{-1}). Consequently, the *syn*-**2-HHTP$_2$** conformer is more stable than *anti*-**2-HHTP$_2$** by 57.5 kJ mol^{-1} and the ferrocene rotation ceases. Further reaction of **2-HHTP$_2$** with another molecule of **2** can lead to either the cage or oligomeric structure. The selectivity of this process strongly depends on molecular conformation. Specifically, the parallel orientation of the **HHTP** molecules in *syn*-**2-HHTP$_2$** enables the fine incorporation of the second ferrocene units to give **2$_2$-HHTP$_2$** (Scheme 2) with a Gibbs free enthalpy of −50.5 kJ mol^{-1}, although the calculations suggest that the reaction proceeds through several elemental steps as depicted in Scheme S1 (ESI†). As the rotation of ferrocene Cp rings in **2-HHTP$_2$** is hampered, the appearance of oligomeric products, in which **HHTP** units are not stacked, can be excluded. Thus, it can be concluded that the main driving force for the formation of the discrete cage structure is the presence of strong dispersive forces, exemplified by the relatively large energy differences between *syn*-**2-HHTP$_2$** and *anti*-**2-HHTP$_2$**. The final reaction of **2$_2$-HHTP$_2$** with the third molecule **2** to give the **FcB-cage** structure is also energetically favoured with ΔG = −76.9 kJ mol^{-1}. The total Gibbs free enthalpy for the generation of the **FcB-cage** from the starting materials is −216.8 kJ mol^{-1} indicating that the process is thermodynamically highly beneficial.

The **FcB-cage** readily precipitates from the solution and the obtained product is sparingly soluble in common organic solvents. This is related to the size of the molecule and its compact character. In addition, it can be expected that cages likely stack on top of each other. According to our calculations, the interaction energy between two molecules **FcB-cage** is equal to 107.6 kJ mol^{-1}, *i.e.*, it is higher by 20.6 kJ mol^{-1} than the intramolecular interaction within the cage. In such a dimeric structure, the intermolecular distance between the neighboured **HHTP** planes is 3.217 Å, which is approximately equal to the distance of two independently π-stacked **HHTP** molecules. At the same time, the molecules are in-plane shifted by 0.382 Å. It is expected that the further propagation of this motif would produce the π-stacking molecular chains.

Conclusions

In conclusion, a novel D_{3h}-symmetric ferrocenylated organic cage bearing boronate ester linkages (**FcB-cage**) has been selectively and effectively synthesized under mild conditions by employing an easy-to-perform reaction. The MAS NMR, ATR-FT-IR, and HRMS analyses supported the structure formulation of the target product as a pure material without traces of oligomeric side-products. The presence of peaks in the low 2θ range in the PXRD pattern implies that the cage crystallizes in large unit cells. In the SEM image, nanocrystallites can be seen whose size coincides with the observed PXRD peak broadenings. It is worth noting that SEM and PXRD analyses were highly consistent and enabled the exclusion of the presence of oligomeric species in the **FcB-cage** sample. The TGA analysis confirmed the high thermal stability of the cage. Lastly, voltammetric analyses revealed that there is electronic communication between the ferrocene units through bonding with a triphenylene core, and since the cage is immobilized on the electrode surface, its electrode processes occur on the surface of the electrode. On the basis of DFT calculations, the molecular structure of the cage was established. Further analysis of the intermediate products enabled us to decipher the reaction mechanism, which explains the selective formation of the cage. By the synthesis of the new ferrocenylated cage bearing boronate ester linkages, this work contributes to the further progress in the synthesis of organized compounds bearing metallocene as a building block.

Experimental

Materials and methods

Chemical reagents and solvents for the synthesis were commercially purchased and purified according to the standard methods, if necessary. Sonication was performed using a Bandelin Sonorex RK 100 H ultrasonic probe with temperature control (ultrasonic peak output/HF power: 320 W/80 W; 35 kHz).

Spectral characterization in solution. The ^{1}H NMR experiments were carried out using an Agilent NMR 400 MHz DDR2 spectrometer. ^{1}H and $^{13}C\{^{1}H\}$ chemical shifts (δ) were reported in parts per million (ppm) relative to TMS by using residual solvent resonances: DMSO-d_6, δ_H (residual DMSO) 2.50 ppm, benzene-d_6, δ_H (residual C_6H_6) 7.16 ppm, δ_C (residual C_6D_5H) 128.4 ppm. The resonances of boron-bound carbon atoms in the $^{13}C\{^{1}H\}$ NMR spectra were not observed as a result of their broadening by a quadrupolar boron nucleus. The ^{11}B chemical shift relative to the $BF_3{\cdot}Et_2O$. NMR spectra were analyzed using the MestReNova v12.0 software (Mestrelab Research S.L).

ESI-HRMS (TOF) experiments. ESI-HRMS (TOF) measurements were performed using a Q-Exactive ThermoScientific spectrometer.

Elemental analysis. Elemental analyses were performed using a CHNS Elementar Vario EL III apparatus. Each elemental composition was reported as an average of two analyses. Elemental analyses were performed for two **FcB-cage** samples from two independent batches, and the elemental composition outcomes of those samples were highly consistent.

MAS NMR measurements. The samples were packed into 3.2 O.D. ZrO_2 rotors. The MAS NMR experiments were performed using an Agilent DirectDrive2 spectrometer (B_0 = 16.4 T, $\nu_L(^{13}C)$ = 176.05 MHz, $\nu_L(^{11}B)$ = 224.62 MHz) with the vnmrJ 4.2 software. A 3.2 mm HXY triple-channel probe under an MAS rate of 12 kHz was used. Referencing was done using the ^{13}C MAS NMR spectrum of adamantane. The ^{11}B spectra were measured using a pulse-acquire sequence with ^{1}H decoupling and the following parameters: ^{11}B $\pi/2$ pulse width 6 μs, spectral width 41 666 Hz, recycle delay 5 s, number of scans 128, and acquisition time 100 ms. The ^{13}C spectra were measured using the CP-MAS sequence with ^{1}H decoupling and the following parameters: ^{13}C: $\pi/2$ pulse width 3.2 μs, ^{1}H: $\pi/2$ pulse width 2.5 μs, spectral width 50 000 Hz, recycle delay 2 s, number of scans 1024, acquisition time 40 ms. All datasets were processed using the Mestrenova 12.0 software, using exponential apodization (100 Hz), zero-filling to 16k points and baseline correction using a polynomial fit of the 3rd order.

ATR-FT-IR analyzes. Fourier-transform infrared (FT-IR) spectra were recorded in the Attenuated Total Reflectance (ATR) mode using a Thermo Nicolet Avatar 370 spectrometer with a spectral resolution of 2 cm^{-1} (80 scans). The wavenumbers for the absorption bands ν were reported in cm^{-1}.

PXRD measurements. Powder X-ray diffraction (PXRD) analyses of the **FcB-cage** (Fig. S16, ESI†), **HHTP** (Fig. S20, ESI†) and **1** (Fig. S19, ESI†) were carried out using a BrukerAXS WAXS D8 powder diffractometer equipped with a Cu radiation source (Cu K_α, λ = 1.54184 Å), a no-background sample holder and a VÅNTEC detector. The samples were placed on the graphite plate and all experiments were performed under air. Data were collected over a 2θ range of 4.1–30° (**FcB-cage**; for 2θ > 30°, no diffraction was observed) or 4.1–40° (**1**, **HHTP**) in Bragg–Brentano geometry with a generator setting of 40 kV and 40 mA, a step size of 0.01°, and an exposure time per step of 6 s. The Pawley refinement for the **FcB-cage** was performed with DASH CCDC (Fig. S17 and S18, ESI†). Two unit cells, *i.e.*, triclinic and monoclinic were proposed (Table S4, ESI†).

SEM and EDS analyses. The scanning electron microscopy (SEM) analyses were performed at low kV electron beam energy (3 kV, 30 pA current). Each sample was covered with a 1–2 nm thin film of Au–Pd alloy before the examination to avoid electrical charging of the sample surface. The layers of the alloy were sputtered using a Polaron SC7620 Mini Sputter Coater. The energy dispersive X-ray spectrometry (EDS) was carried out using a multichannel device, EDS XFlash Detector 5010 125 eV, Quantax (Bruker, Germany) using 10 kV electron beam energy.

TGA/DSC. Thermal analysis was performed using a TGA/DSC1 (Mettler-Toledo) system under a continuous flow of argon at T = 30–600 °C with a ramp rate of 10 K min^{-1}. The sample was prepared in a covered ceramic crucible. An empty crucible was used as a reference. α-Al_2O_3 was used for instrument calibration. The measurement was carried out after preliminary drying at 85 °C under 0.1 Torr for 24 h.

Voltammetric analysis. Cyclic voltammetry (CV) experiments were performed using an Autolab Eco Chemie potentiostat, model PGSTAT 12. The studies were performed in a three-electrode system. The disc glassy carbon electrode (GC, ϕ = 3 mm, BAS Instruments) was used as a working electrode, Ag/AgCl/3 M KCl was used as the reference electrode, and a platinum wire was used as the auxiliary electrode. To minimize the electrical noise, the electrochemical cell was kept in a Faraday cage. The HOMO energy level was determined from the first oxidative potential value using the equation: $E_{HOMO} = -(E_{ox} + 5.1\ eV)$. The **FcB-cage** is characterized by high sensitivity to moisture. Therefore, a dry solvent was used and the measurements were carried out under anhydrous conditions in the presence of molecular sieves. The electrode modification procedure was very simple and was based on adding a 7 μL droplet of the **FcB-cage** (5 mM well dispersed suspension in 1-octanol with the addition of 0.10 M tetrabutylammonium tetrafluoroborate ($TBABF_4$) and 0.5% Nafion®) on the electrode surface and allowing it to dry in the desiccator.

Synthesis

1,1′-Ferrocenediboronic acid (1). This compound was prepared by dilithiation of ferrocene with *n*-BuLi/TMEDA and subsequent boronation according to the slightly modified literature procedure ($B(OMe)_3$ was used instead of $B(OBu)_3$).[33] Yield 59%. The ^{1}H NMR spectrum of the product conforms to that reported previously:[49] ^{1}H NMR (400 MHz, DMSO-d_6) δ 7.47 (s, 4H), 4.34 (t, J = 1.8 Hz, 4H), 4.17 (t, J = 1.8 Hz, 4H) ppm.

1,1′-Bis(dimethoxyboryl)ferrocene (2). 1,1′-Ferrocenediboronic acid (**1**; 1.78 g, 6.0 mmol) was suspended in Et_2O (10 mL). Methanol (3 mL), trimethyl orthoformate (2 mL, 20 mmol) and HCl (2 M in Et_2O, 0.05 mL) were added. The mixture was stirred for 1 hour at room temperature. The solvents were removed under reduced pressure and the residue was redissolved in dry hexane (35 mL) under an argon atmosphere. An orange solution was carefully transferred with a syringe (a small amount of an insoluble material remained in a flask) to

a Schlenk tube which was previously evacuated and back-filled with argon. The solution was concentrated under reduced pressure to leave the residue which was subjected to high vacuum (10^{-3} mbar, 40 °C, *ca.* 3 hours) in order to remove traces of solvents and volatile reagents. Product **2** was obtained as a viscous red oil. Yield 2.05 g (96%). ^{1}H NMR (400 MHz, benzene-d_6) δ 4.53 (t, J = 1.6 Hz, 4H), 4.27 (t, J = 1.6 Hz, 4H), 3.64 (s, 12H) ppm. ^{13}C NMR (101 MHz, benzene-d_6) δ 75.7, 72.8, 52.2 ppm. ^{11}B NMR (96 MHz, benzene-d_6) δ 28.5 ppm.

Optimized procedure for the synthesis of FcB-cage. 1,1′-Bis (dimethoxyboryl)ferrocene (**2**; 151.2 mg, 0.459 mmol) and **HHTP** (102.5 mg, 0.316 mmol) were dissolved in DMF (40 ml). The reaction mixture was stirred for 48 hours at room temperature. A light brown solid started to precipitate after *ca.* 15–30 minutes. The precipitate was then filtered off and washed with DMF. The solid product was suspended in DMF (30 mL), sonicated at room temperature for several minutes, and filtered off. The procedure was repeated once with the use of acetone (30 mL). The resultant solid was dried in a vacuum to obtain the **FcB-cage** (130 mg; 68%) in the form of dark-grey solid.

^{13}C MAS NMR (176.05 MHz, ppm) δ 150.4, 128.2, 108.6, 77.5; ^{11}B MAS NMR (224.62 MHz, ppm) δ 24.9; ATR-FT-IR, ν 1387, 1321, 1292, 1245, 1162, 1117, 1059, 1027 cm^{-1}; TOF-HRMS (ESI): calcd for $C_{66}H_{37}B_6Fe_3O_{12}$ $[M + H]^+$ = 1254.0922, found: *m*/*z* 1254.0922; EDS: B, 6.22; C, 61.46; O, 20.9; Fe, 11.3 wt%; Elem. anal. calcd for $C_{66}H_{36}B_6Fe_3O_{12}$: C, 63.25; H, 2.90, found: C, 58.86; H, 3.35.

Hydrolysis experiment with FcB-cage. Solid **FcB-cage** (25 mg) was suspended in DMSO-d_6 (1 mL). The mixture was stirred for 24 hours at room temperature in air. It was then filtered off (syringe filter 0.22 μm) directly to the NMR tube, and the ^{1}H NMR spectrum was measured.

^{1}H NMR (DMSO-d_6, 400 MHz, ppm), δ 9.77 (s, 12H; O–**H**, **HHTP**), 7.60 (s, 12H; Ar–**H**, **HHTP**), 7.46 (s, 12H; B(O**H**)$_2$, **1**), 4.34 (t, J = 1.8 Hz, 12H; Cp–**H**, **1**), 4.17 (t, J = 1.8 Hz, 12H; Cp–**H**, **1**). *The calculated molar ratio of **1**:**HHTP** is 3 : 2.*

Theoretical calculations

Theoretical calculations were performed using the Gaussian16 program.[50] Molecules were optimized using the B97D functional[51] (DFT) with 6-311++G(d,p) basis set.[52] As the crystal data was not available for the **FcB-cage**, the initial structure was generated manually in the GaussView program.[53] The initial structure of **2** was built based on the crystal structure of **1** by the substitution of hydrogen atoms with methyl groups. There are two polymorphic forms of **1**; in one form, the boronic groups are in the *syn* conformation with respect to each other,[54] while in the second they are in the *anti* position due to the rotation of the Cp rings.[55] Thus, the initial structures of *syn*-**2** and *anti*-**2** conformers were constructed based on the molecular geometries derived from the corresponding crystal structures of **1**. According to our computations, the *syn* and *anti* rotamers of **2** are equally stabilized in solution (ΔE = 0.1 kJ mol^{-1}) and the interconversion energy barrier is below 4 kJ mol^{-1}, which is in line with a very small energy barrier for Cp rotation in ferrocene and its derivatives. The introduction of the boronic group has a marginal effect on Cp ring rotation unless it is hampered by the strong intramolecular interactions as is observed for the **2-HHTP$_2$** intermediate. In the next step, several different conformations of boronic groups namely, *syn–syn*, *syn–anti*, and *anti–anti* were considered (Fig. S10, ESI†). According to our results, the *syn–anti* conformation of the boronic ester group is the most favoured, which is the common feature for the number of boronic acids and their derivatives.[56,57] The rotation of the boronic ester group around the B–C bond was calculated using the scan procedure in Gaussian (other parameters were optimised during the scan procedure). The calculated energy barrier is 33 kJ mol^{-1}. The most stable conformation of **2** was taken for the subsequent calculation of the reaction mechanism. The intermediate structures *en route* to the final product **FcB-cage** were initially built using the GaussView programme and then subjected to the optimisation procedure. Following geometry optimization, the vibrational frequencies were calculated and the results showed that the optimized structures are stable geometric structures (no imaginary frequencies, Table S3, ESI†). In the optimization processes, no symmetry constraints were applied. The molecular volume of the **FcB-cage** was calculated with Gaussian using the keyword 'volume', which defines the volume inside the electron density isosurface of 0.001 e bohr^{-1}.[3] Gibbs free energies were obtained from the frequency calculations with the temperature set to 298 K. To take into account the experimental conditions all calculations were performed in the presence of the solvent field with the polarizable continuum model (PCM) using the CPCM polarizable conductor calculation model and DMF was used as the solvent.[58] The geometries of the optimized structures are provided in the ESI (Fig. S8–S10†) as well as the supplementary .xyz format file. The dimer interaction energies were calculated using the supermolecular method including Basis Set Superposition Error (BSSE). The intramolecular interaction energy between the **HHTP** units in the **FcB-cage** was calculated after extracting ferrocene moieties from the structure of the B–C bonds. The boron atoms were terminated with the hydrogen atoms. The **FcB-cage** dimer was freely optimized prior to the intermolecular energy calculations (Fig. S14, ESI†).

Conflicts of interest

There are no conflicts to declare.

Acknowledgements

Financial support from the Warsaw University of Technology is acknowledged. The publication and M. K.'s contribution are a part of the "Szkoła Orłów" project, co-financed by the European Social Fund under the Knowledge-Education-Development Operational Programme, Axis III, Higher Education for the Economy and Development, Measure 3.1,

Competences In Higher Education. This work was supported by the National Science Centre (Poland) within the framework of the project DEC-UMO-2016/21/B/ST5/00118 (K. D., S. L.). The authors thank Wroclaw Centre for Networking and Supercomputing (http://www.wcss.pl), grant No. 285, for providing computer facilities (Gaussian16).

References

1 S. Wan, J. Guo, J. Kim, H. Ihee and D. Jiang, *Angew. Chem., Int. Ed.*, 2008, **47**, 8826–8830.
2 E. L. Spitler and W. R. Dichtel, *Nat. Chem.*, 2010, **2**, 672–677.
3 K. Gontarczyk, W. Bury, J. Serwatowski, P. Wieciński, K. Woźniak, K. Durka and S. Luliński, *ACS Appl. Mater. Interfaces*, 2017, **9**, 31129–31141.
4 P. Pacholak, K. Gontarczyk, R. Kamiński, K. Durka and S. Luliński, *Chem. – Eur. J.*, 2020, **26**, 12688–12688.
5 E. L. Spitler, B. T. Koo, J. L. Novotney, J. W. Colson, F. J. Uribe-Romo, G. D. Gutierrez, P. Clancy and W. R. Dichtel, *J. Am. Chem. Soc.*, 2011, **133**, 19416–19421.
6 A. P. Côté, A. I. Benin, N. W. Ockwig, M. O'Keeffe, A. J. Matzger and O. M. Yaghi, *Science*, 2005, **310**, 1166–1170.
7 B. J. Smith, N. Hwang, A. D. Chavez, J. L. Novotney and W. R. Dichtel, *Chem. Commun.*, 2015, **51**, 7532–7535.
8 K. Geng, T. He, R. Liu, S. Dalapati, K. T. Tan, Z. Li, S. Tao, Y. Gong, Q. Jiang and D. Jiang, *Chem. Rev.*, 2020, **120**, 8814–8933.
9 J. W. Colson and W. R. Dichtel, *Nat. Chem.*, 2013, **5**, 453–465.
10 S. Bi, C. Yang, W. Zhang, J. Xu, L. Liu, D. Wu, X. Wang, Y. Han, Q. Liang and F. Zhang, *Nat. Commun.*, 2019, **10**, 2467.
11 E. Jin, J. Li, K. Geng, Q. Jiang, H. Xu, Q. Xu and D. Jiang, *Nat. Commun.*, 2018, **9**, 4143.
12 N. Huang, L. Zhai, D. E. Coupry, M. A. Addicoat, K. Okushita, K. Nishimura, T. Heine and D. Jiang, *Nat. Commun.*, 2016, **7**, 12325.
13 H. Ding, J. Li, G. Xie, G. Lin, R. Chen, Z. Peng, C. Yang, B. Wang, J. Sun and C. Wang, *Nat. Commun.*, 2018, **9**, 5234.
14 A. I. Cooper, *ACS Cent. Sci.*, 2017, **3**, 544–553.
15 T. Kunde, T. Pausch and B. M. Schmidt, *Chem. – Eur. J.*, 2021, **27**, 8457–8460.
16 T. Tozawa, J. T. A. Jones, S. I. Swamy, S. Jiang, D. J. Adams, S. Shakespeare, R. Clowes, D. Bradshaw, T. Hasell, S. Y. Chong, C. Tang, S. Thompson, J. Parker, A. Trewin, J. Bacsa, A. M. Z. Slawin, A. Steiner and A. I. Cooper, *Nat. Mater.*, 2009, **8**, 973–978.
17 T. Kunde, E. Nieland, H. V. Schröder, C. A. Schalley and B. M. Schmidt, *Chem. Commun.*, 2020, **56**, 4761–4764.
18 X. Li, C. Yang, B. Sun, S. Cai, Z. Chen, Y. Lv, J. Zhang and Y. Liu, *J. Mater. Chem. A*, 2020, **8**, 16045–16060.
19 K. Severin, *Dalton Trans.*, 2009, 5254.
20 R. Nishiyabu, Y. Kubo, T. D. James and J. S. Fossey, *Chem. Commun.*, 2011, **47**, 1124–1150.
21 J. K. Day, C. Bresner, I. A. Fallis, L.-L. Ooi, D. J. Watkin, S. J. Coles, L. Male, M. B. Hursthouse and S. Aldridge, *Dalton Trans.*, 2007, 3486.
22 K. Tamaki, A. Ishigami, Y. Tanaka, M. Yamanaka and K. Kobayashi, *Chem. – Eur. J.*, 2015, **21**, 13714–13722.
23 T. K. Ronson, J. P. Carpenter and J. R. Nitschke, *Chem*, 2022, **8**, 557–568.
24 N. Schäfer, M. Bühler, L. Heyer, M. Röhr and F. Beuerle, *Chem. – Eur. J.*, 2020, **27**, 6077–6085.
25 K. Kataoka, T. D. James and Y. Kubo, *J. Am. Chem. Soc.*, 2007, **129**, 15126–15127.
26 Z. Shan, X. Wu, B. Xu, Y. Hong, M. Wu, Y. Wang, Y. Nishiyama, J. Zhu, S. Horike, S. Kitagawa and G. Zhang, *J. Am. Chem. Soc.*, 2020, **142**, 21279–21284.
27 E. Giraldi, R. Scopelliti, F. Fadaei-Tirani and K. Severin, *Inorg. Chem.*, 2021, **60**, 10873–10879.
28 A. Kasprzak and P. A. Guńka, *Dalton Trans.*, 2020, **49**, 6974–6979.
29 A. I. Kosińska, M. K. Nisiewicz, A. M. Nowicka and A. Kasprzak, *ChemPlusChem*, 2021, **86**, 820–826.
30 D. Astruc, *Eur. J. Inorg. Chem.*, 2017, **2017**, 6–29.
31 B. Gélinas, T. Bibienne, M. Dollé and D. Rochefort, *Can. J. Chem.*, 2020, **98**, 554–563.
32 C. Bravin, A. Guidetti, G. Licini and C. Zonta, *Chem. Sci.*, 2019, **10**, 3523–3528.
33 T.-H. Chen, W. Kaveevivitchai, N. Bui and O. Š. Miljanić, *Chem. Commun.*, 2012, **48**, 2855.
34 R. L. Li, N. C. Flanders, A. M. Evans, W. Ji, I. Castano, L. X. Chen, N. C. Gianneschi and W. R. Dichtel, *Chem. Sci.*, 2019, **10**, 3796–3801.
35 M. Scheibitz, M. Bolte, J. W. Bats, H.-W. Lerner, I. Nowik, R. H. Herber, A. Krapp, M. Lein, M. C. Holthausen and M. Wagner, *Chem. – Eur. J.*, 2005, **11**, 584–603.
36 L. M. Salonen, D. D. Medina, E. Carbó-Argibay, M. G. Goesten, L. Mafra, N. Guldris, J. M. Rotter, D. G. Stroppa and C. Rodríguez-Abreu, *Chem. Commun.*, 2016, **52**, 7986–7989.
37 H. Nöth and B. Wrackmeyer, *Nuclear Magnetic Resonance Spectroscopy of Boron Compounds*, Springer Berlin Heidelberg, Berlin, Heidelberg, 1978.
38 M. K. Smith and B. H. Northrop, *Chem. Mater.*, 2014, **26**, 3781–3795.
39 I. H. Sarker, *SN Comput. Sci.*, 2021, **2**, 160.
40 X. F. Cadet, O. Lo-Thong, S. Bureau, R. Dehak and M. Bessafi, *Sci. Rep.*, 2019, **9**, 19197.
41 N. Artrith, K. T. Butler, F.-X. Coudert, S. Han, O. Isayev, A. Jain and A. Walsh, *Nat. Chem.*, 2021, **13**, 505–508.
42 J. Cervantes, F. Garcia-Lamont, L. Rodríguez-Mazahua and A. Lopez, *Neurocomputing*, 2020, **408**, 189–215.
43 R. J. LeSuer and W. E. Geiger, *Angew. Chem., Int. Ed.*, 2000, **39**, 248–250.
44 A. Simonova, I. Magriñá, V. Sýkorová, R. Pohl, M. Ortiz, L. Havran, M. Fojta, C. K. O'Sullivan and M. Hocek, *Chem. – Eur. J.*, 2020, **26**, 1286–1291.
45 H. Fink, N. J. Long, A. J. Martin, G. Opromolla, A. J. P. White, D. J. Williams and P. Zanello, *Organometallics*, 1997, **16**, 2646–2650.

46 B. Wang and J. Anzai, *Int. J. Electrochem. Sci.*, 2015, **10**, 3260–3268.
47 K. Lehmann, O. Yurchenko and G. Urban, *J. Phys.: Conf. Ser.*, 2014, **557**, 012008.
48 K. Ono, Y. Tohyama, T. Uchikura, Y. Kikuchi, K. Fujii, H. Uekusa and N. Iwasawa, *Dalton Trans.*, 2017, **46**, 2370–2376.
49 R. Knapp and M. Rehahn, *J. Organomet. Chem.*, 1993, **452**, 235–240.
50 M. J. Frisch, G. W. Trucks, H. B. Schlegel, G. E. Scuseria, M. A. Robb, J. R. Cheeseman, G. Scalmani, V. Barone, G. A. Petersson, H. Nakatsuji, X. Li, M. Caricato, A. V. Marenich, J. Bloino, B. G. Janesko, R. Gomperts, B. Mennucci, H. P. Hratchian, J. V. Ortiz, A. F. Izmaylov, L. Sonnenberg, D. Williams-Young, F. Ding, F. Lipparini, F. Egidi, J. Goings, B. Peng, A. Petrone, T. Henderson, D. Ranasinghe, V. G. Zakrzewski, J. Gao, N. Rega, G. Zheng, W. Liang, M. Hada, M. Ehara, K. Toyota, R. Fukuda, J. Hasegawa, M. Ishida, T. Nakajima, Y. Honda, O. Kitao, H. Nakai, T. Vreven, K. Throssell, J. A. Montgomery, Jr., J. E. Peralta, F. Ogliaro, M. J. Bearpark, J. J. Heyd, E. N. Brothers, K. N. Kudin, V. N. Staroverov, T. A. Keith, R. Kobayashi, J. Normand, K. Raghavachari, A. P. Rendell, J. C. Burant, S. S. Iyengar, J. Tomasi, M. Cossi, J. M. Millam, M. Klene, C. Adamo, R. Cammi, J. W. Ochterski, R. L. Martin, K. Morokuma, O. Farkas, J. B. Foresman and D. J. Fox, 2016.
51 S. Grimme, *J. Comput. Chem.*, 2006, **27**, 1787–1799.
52 C. Lee, W. Yang and R. G. Parr, *Phys. Rev. B: Condens. Matter Mater. Phys.*, 1988, **37**, 785–789.
53 R. Dennington, T. Keith and J. Milla, GaussView, Version 6.1.1, Semichem Inc., Shawnee Mission, KS, 2019.
54 M. Bolte, CSD Communication(Private Communication), 2011, Refcode: OBEBUU.
55 G. J. Palenik, *Inorg. Chem.*, 1969, **8**, 2744–2749.
56 I. D. Madura, K. Czerwińska and D. Sołdańska, *Cryst. Growth Des.*, 2014, **14**, 5912–5921.
57 K. Durka, K. N. Jarzembska, R. Kamiński, S. Luliński, J. Serwatowski and K. Woźniak, *Cryst. Growth Des.*, 2012, **12**, 3720–3734.
58 J. Tomasi, B. Mennucci and R. Cammi, *Chem. Rev.*, 2005, **105**, 2999–3094.